Front. Earth Sci. 2024, 18(4): 752−762
https://doi.org/10.1007/s11707-024-1113-2

RESEARCH ARTICLE

Case studies of hailstorms in Shandong Province using hail size discrimination algorithm based on dual polarimetric parameters

Juxiu WU[1,5], Fan XIA (✉)[2,5,7], Jiawen PAN[3,6], Guanglu HAN[1], Weijia SUN[1], Chen GU[4]

1 Shandong Meteorological Engineering Technology Center, Jinan 250031, China
2 Meteorological Sciences Institute of Shandong, Jinan 250031, China
3 Xiamen Meteorological Bureau, Xiamen 361012, China
4 College of Geodesy and Geomatics, Shandong University of Science and Technology, Qingdao 266590, China
5 Key Laboratory for Meteorological Disaster Prevention and Mitigation of Shandong, Jinan 250031, China
6 Xiamen Key Laboratory of Straits Meteorology, Xiamen 361012, China
7 Changdao National Climate Observatory, Changdao 265800, China

Abstract The hail size discrimination algorithm (HSDA) and its capacity to identify hail in Shandong Province are analyzed to satisfy the localized requirement by China's S-band dual-polarization radars. A modified HSDA is obtained by using optimized membership function thresholds based on the statistics of Shandong hail data. The results are verified by a supercell storm process. 1) The modified HSDA improves the identification of large hail and giant hail. The results are consistent with the analysis of the scattering and polarization parameter characteristics of different-size hails, the dynamic and microphysical characteristics for supercell, and the real situation. 2) The horizontal and vertical hail-size distribution characteristics are consistent with the analysis about the growth process of larger hails and the precipitation particles filtering mechanisms in supercells. Small hail first forms at the suspension echo, then is injected into the larger hail growth area above the bounded weak echo area driven by updrafts, colliding with the abundant supercooled water in the K_{DP} column. Finally, large hail and giant hail fall near the direction of the updrafts to form a strong echo wall, and giant hail falls 6–12 km from the central updraft. 3) The maxima of the Z_{DR} and K_{DP} columns can be used to predict the hail-growth trend, which exceeds the −20°C isotherm for the heavy-hail growth stage at high-altitude in the supercell storm. When hail falls to the ground, the Z_{DR} column shortens and the K_{DP} column disappears, which provides the observation basis from polarimetric radars for the consumption of supercooled water by hail growth.

Keywords polarimetric parameters, hail size discrimination, membership function, giant hail

Received June 20, 2023; accepted December 13, 2023

E-mail: xf0718@126.com

1 Introduction

Hail disasters are severe meteorological disasters induced by severe convective weather. Hail usually happens unexpectedly, accompanied by disastrous weather processes such as strong wind and heavy rain, usually resulting in significant losses to lives and property. The size of hail correlates directly with the extent of hail disasters. Large hailstones (i.e., diameter > 2 cm) can cause serious damage to crops, and so are the focus of hail warnings and forecasts. At present, hail-size estimation via Chinese operational dual-polarization radar is still derived from the hail algorithm based on single-polarization radar (Witt et al., 1998). Diao et al. (2007) found that the average difference between the predicted and actual sizes of 13 individual hail cells was about 1.46 cm, which shows that this algorithm overestimates the hail size.

Compared with single-polarization radar, the polarimetric parameters, such as the differential reflectivity factor Z_{DR} and the correlation coefficient (CC) of dual-polarization radars, offer significant advantages in hail recognition (Zrnić and Ryzhkov, 1999; Heinselman and Ryzhkov, 2006; Dolan and Rutledge, 2009), and the hydrometeor classification algorithm (HCA; Park et al., 2009) based on fuzzy logic method and adopted by operational dual-polarization radars can identify ten types of hydrometeors

including hail or mixed hail and rain. Scharfenberg et al. (2005) reviewed the polarization algorithms for rainfall estimation and HCA used in American operational radars and evaluated their performance through joint polarization experiments. Snyder et al. (2014) analyzed the dual polarization characteristics of X-band and S-band radar detection in two supercell storms. Wu et al. (2018) adjusted the weight factor and membership-function threshold in the HCA developed by Park et al. (2009) according to the Zhuhai radar detection data, obtaining a localized hydrometeor discrimination algorithm. Al-Sakka et al. (2013) developed a new fuzzy logic method to identify S-, C-, and X-band dual-polarization radar hydrometeors by using observed data from French radar and T-matrix simulation data for radar measurements of deviation, noise, and temperature.

The relationship between hail size and polarimetric parameters has been studied worldwide. Kaltenboeck and Ryzhkov (2013) made a comparative analysis of hail data acquired in Oklahoma, USA by S- and C-band dual-polarized radars and found that the polarization radar variables of the two radars differ significantly, which became especially noticeable when the hail melted. In addition, they also analyzed the average vertical profiles of polarization parameters for hailstones with diameters of 2, 4, and 10 cm. Based on the T-matrix algorithm and the one- and two-dimensional cloud models, Ryzhkov et al. (2013a) simulated the polarization characteristics of hail parameters and analyzed the vertical profiles of S-, C-, and X-band dual-polarization parameters as functions of hail or graupel particle size. The NOAA National Severe Storms Laboratory of the USA developed the hail size discrimination algorithm (HSDA) to replace the particle phase classification algorithm currently used by the S-band radar network (NEXRAD) (Ryzhkov et al., 2013b), and three types of hail were identified in six height layers based on the fuzzy logic method. The HSDA validation was performed using radar data collected by numerous WSR-88D sites and more than 3000 surface hail reports obtained from the Severe Hazards Analysis and Verification Experiment (Ortega et al., 2016), which demonstrates that HSDA outperforms the currently running single-polarization hail-detection algorithm.

At present, the China Meteorological Administration has completed the polarization upgrade of nearly 100 radars, but the operational dual-polarization radar still uses the hail size identification algorithm from single-polarization radar. The studies of hail based on polarization radar in China are mostly concentrated on hail case, the evolution of dynamic microphysical characteristics of hail clouds, and the characteristics of the polarization parameters of hail (Wang et al., 2018; Lin et al., 2020; Pan et al., 2020, 2021; Diao and Guo, 2021; Diao et al., 2021), whereas few studies in China use the algorithm of hail size based on polarimetric parameters. Given that more polarimetric radars will be used in future operational weather services, developing HSDA for domestic radars and hail weather processes becomes an urgent task. For this reason, we summarize the location, occurrence time, hail size, and their corresponding polarimetric parameters from Shandong Province in the past two years. We then investigate the polarimetric characteristics of hail by dividing the hail sizes into three categories: small hail, large hail, and giant hail (Wu et al., 2022). To do this, we use the HSDA of Ortega et al. (2016) and study its suitability for Shandong. The localized trapezoidal membership function threshold is then determined preliminarily, and the modified HSDA is verified by applying it to a hailstorm (17 May, 2020) with multiple supercells.

2 Basic theory and methods

The hail size discrimination algorithm (HSDA) (Ortega et al., 2016) uses a fuzzy-logic scheme to calculate an aggregation. First, a membership function is established for each category based on experience and observation statistics. Figure 1 shows the trapezoidal membership function, where $P(X)$ is a radar observation datum plotted against a certain type of probability distribution in the interval X_1–X_4. Each membership function is accumulated to obtain an aggregate value, as seen in

$$A_i = \frac{\sum_{j=1}^{3} W_{ij} Q_j P_i\left(V_j\right)}{\sum_{j=1}^{3} W_{ij} Q_j}, \tag{1}$$

where V_j is the jth variable. The input variables V_1, V_2, and V_3 refer to the horizontal reflectivity factor Z_H, the differential reflectivity factor Z_{DR} and the CC, respectively. $P_i(V_j)$ is the membership function for the jth variable, which describes the distribution of the jth variable in the ith category. The value of the trapezoidal membership function is determined by the relative position between the input variable and the trapezoidal membership function parameters, and different parameters correspond to the distributions of polarimetric parameters of different categories. Q_j is a confidence

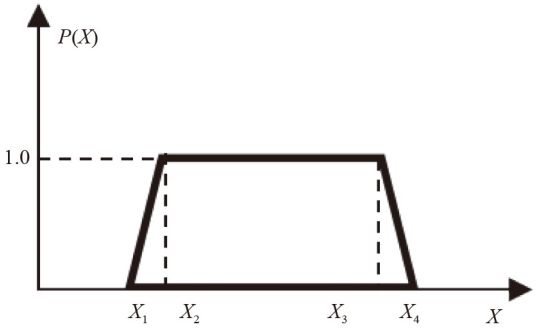

Fig. 1 Trapezoidal membership function.

factor that explains the influence on the jth variable of radar measurement error, such as attenuation, beam blocking, or uneven beam filling. Given that measurement error is not considered in this paper, the weight Q_j is taken as 1. W_{ij} is the weight assigned to the jth variable and varies from zero to unity. It describes the identification ability of each variable of a specific category.

The membership degree A_i of the ith category is obtained by accumulating, and then the membership degrees of all categories are compared. The classification of the maximum membership degree A_i is the classification result of the input variables. Ortega et al. (2016) classified the hail size according to the U.S. hail grading standard into small hail (diameter <2.5 cm), large hail (5 cm ⩾ diameter ⩾ 2.5 cm), and giant hail (diameter > 5 cm).

3 Localization of HSDA proposed by Ortega et al. (2016)

3.1 Classification of hail size and division of height layer

Because the occurrence frequency and intensity of hail in China are generally less severe than in the USA, the three types of hail are categorized as small hail (diameter < 2.0 cm), large hail (5 cm > diameter ⩾ 2 cm), and giant hail (diameter ⩾5 cm) based on China's Standard for Hail Grades (GB/T 27957-2011) (Zeng et al., 2019). The data on hailstone size used in this article are mainly from disaster reports submitted by observation stations and eyewitness reports extracted from the WeChat applet "Hail Chaser" developed by the Shandong Weather Modification Office.

To refine the polarization-parameter characteristics of hail at different altitudes, the sounding data of hail events with similar temporal and spatial scales are selected, and the vertical height is divided into seven altitude intervals based on the heights of wet bulb temperature at 0°C, −10°C, and −20°C (Pan et al., 2021). The specific height intervals are given in Table 1. Yu (2014) used the wet bulb 0°C isotherm as the initial height of hail melting, and the data points were classified into corresponding altitude intervals by location of the center of the radar sampling volume, so each altitude interval has a corresponding membership function.

3.2 The modification of membership function thresholds

The radar data are obtained from the S-band dual-polarization radars in Jinan and Qingdao. Given that the data quality of radar polarization parameters strongly affects the recognition results, the data were first subjected to quality control. The non-meteorological echoes such as clear air echo and ground echo are filtered out based on the dpQC scheme (Tang et al., 2014; Xia et al., 2021). Based on experience and the polarization parameter distribution characteristics of hail in seven altitude layers from previous studies (Wu et al., 2022), and combined with the research results of Ortega et al. (2016), threshold values of membership function are preliminarily determined. The final values are then determined through continuous debugging, as listed in Table 2. Compared with previous research (Ortega et al., 2016), the thresholds of horizontal reflectivity factor Z_H at all altitude intervals and Z_{DR} above the melting layer are primarily modified. The CC mainly takes the published thresholds. Finally, at 1 km below the 0°C layer and lower height, Z_{DR} is related to Z_H. Therefore, the membership function Z_{DR} below the melting layer is taken from the research results of Ortega et al. (2016). The variables are shown in Eqs. (2)–(7) and Z_{DR} for each interval are the variable functions f_1, f_2, f_3, g_1, g_2, g_3, respectively (Ortega et al., 2016).

$$f_1 = -0.5 + 2.5\times10^{-3}\times Z_H + 7.5\times10^{-4}\times H^2 + \Delta Z_{DR}, \quad (2)$$

$$f_2 = 0.1\times(Z_H - 50) + \Delta Z_{DR}, \quad (3)$$

$$f_3 = 0.1\times(Z_H - 60) + \Delta Z_{DR}, \quad (4)$$

$$g_1 = -0.9 + 1.5\times10^{-2}\times Z_H + 5.0\times10^{-4}\times {Z_H}^2 + \Delta Z_{DR}, \quad (5)$$

$$g_2 = 0.075\times(Z_H - 50) + \Delta Z_{DR}, \quad (6)$$

$$g_3 = 0.075\times(Z_H - 60) + \Delta Z_{DR}. \quad (7)$$

The value of ΔZ_{DR} in Eqs. (2)–(7) can be adjusted according to the specific weather process and usually falls between −0.5 dB and 0 dB (Ortega et al., 2016). The larger ΔZ_{DR} is, the larger or more giant hailstones are in the same weather process, and the Z_{DR} calibration differences caused by the different radars can also be corrected by changing ΔZ_{DR}. The weights of each variable at the seven altitude layers are based on the results of Ortega et al. (2016) and Park et al. (2009). The member-

Table 1 Information of altitude intervals

Height class	Range of height class
H_7	$H_h \geqslant H_{-20°C}$
H_6	$H_{-10°C} \leqslant H_h < H_{-20°C}$
H_5	$H_{0°C} \leqslant H_h < H_{-10°C}$
H_4	$H_{0°C}$−1 km$\leqslant H_h < H_{0°C}$
H_3	$H_{0°C}$−2 km$\leqslant H_h < H_{0°C}$−1 km
H_2	$H_{0°C}$−3 km$\leqslant H_h < H_{0°C}$−2 km
H_1	$H_{0°C}$−3 km$> H_h$

Notes: H_h represents the heights of hail, $H_{0°C}$, $H_{-10°C}$, $H_{-20\,°C}$ show the heights of wet bulb temperature at 0°C, −10°C, −20°C, and $H_{0°C}$−1 km, $H_{0°C}$−2 km, and $H_{0°C}$−3 km show the heights at 1 km, 2 km, and 3 km below the 0°C layer, respectively.

Table 2 Membership functions of three types of hails at different altitudes

Height class	Z_H			Z_{DR}			CC		
	Small hail x_1,x_2,x_3,x_4	Large hail x_1,x_2,x_3,x_4	Giant hail x_1,x_2,x_3,x_4	Small hail x_1,x_2,x_3,x_4	Large hail x_1,x_2,x_3,x_4	Giant hail x_1,x_2,x_3,x_4	Small hail x_1,x_2,x_3,x_4	Large hail x_1,x_2,x_3,x_4	Giant hail x_1,x_2,x_3,x_4
H_7	45,50,60,65	48,55,65,68	55,60, 80,85	−0.5,−0.3, 0.3,0.8	−0.6,−0.3, 0.3,0.8	−10,−7.75, 0.3,0.5	0.92,0.96,0.99,1	0.92,0.96,0.99,1	0,0.5, 0.99,1
H_6	45,50,60,66	48,58,65,68	55,62, 80,85	−0.6,−0.3, 0.3,0.8	−0.6,−0.3, 0.3,0.8	−10,−7.75, 0.2,0.5	0.92,0.96,0.99,1	0.86,0.90,0.96,0.98	0,0.5, 0.93,0.98
H_5	46,50,62,67	48,58,66,70	55,65, 80,85	−0.5,−0.3, 0.3,0.8	−1,−0.3, 0.3,0.8	−10,−7.75, 0.2,0.8	0.92,0.96,0.99,1	0.86,0.90,0.96,0.98	0,0.5, 0.93,0.98
H_4	46,50,62,67	50,58, 66,70	58,68, 80,85	−0.1, 0.3, 0.7,1.5	−0.3, 0.1, 0.5,1.3	−10,−7.75, 0.2,0.8	0.93,0.96,0.99,1	0.8,0.91,0.97,0.98	0,0.5, 0.94,0.98
H_3	48,55,62,70	50,62,67,72	62,68, 80,85	g_2−0.3, g_2, g_1,g_1+0.3	g_3−0.3, g_3, g_2,g_2+0.3	−10,−7.75, g_3,g_3+0.3	0.94,0.96,0.98,1	0.8,0.91,0.97,0.98	0,0.5, 0.96,0.98
H_2	48,52,60,65	50,60,65,70	60,66, 80,85	f_2−0.3, f_2, f_1,f_1+0.3	f_3−0.3, f_3, f_2,f_2+0.3	−10,−7.75, f_3,f_3+0.3	0.91,0.94,0.96,0.99	0.8,0.9,0.96,0.99	0,0.5, 0.93,0.98
H_1	48,50,58,63	50,58,63,68	60,65, 80,85	f_2−0.3, f_2, f_1,f_1+0.3	f_3−0.3, f_3, f_2,f_2+0.3	−10,−7.75, f_3,f_3+0.3	0.91,0.94,0.96,0.99	0.8,0.9,0.96,0.99	0,0.5, 0.93,0.98

ship thresholds and degree of small hail are enlarged in localized HSDA. The lowest Z_H threshold for small hail in the lowest layer increases from 45 dBZ of Ortega et al. (2016) to 48 dBZ. Still, the thresholds for large hail change little, and those for giant hail are modified from (50, 59, 100, 101) to (60, 65, 80, 85) because statistics (Wu et al., 2022) showed that the hail reflectivity factor detected by Shandong radars did not exceed 80 dBZ.

3.3 Comparative analysis of recognition results proposed by Ortega et al. (2016) and the modified HSDA

The HCA (Park et al., 2009) was first used to recognize the hail range, and then the modified HSDA was applied in the given hail range where the heavy hail occurred, including in the towns of Shengzhuang, Cu'ai, and Yangliu in Shandong Province. The hail lasted between 5 and 20 minutes, with small amounts of hail having maximum diameters of 4 to 5 cm and most of the hail having diameters of 2 to 3 cm at 18:00 to 18:20 on June 1, 2020, Beijing Standard Time (BST). The hail sizes detected by the HSDA proposed by Ortega et al. (2016) and the modified HSDA with $\Delta Z_{DR} = -0.5$ dB and rR the polarimetric parameters at 1.5° elevation from the Jinan radar at 18:05 are distinguished in Fig. 2, which shows that, based on the modified HSDA, the large hail area increases while the giant hail area decreases (Figs. 2(a1)–2(c1), 2(a2)–2(c2)) at each elevation angle (although little difference occurs at 0.5° elevation). This result is more consistent with reality. According to eyewitnesses, the hail began to fall at 18:00 and lasted for about 5 minutes in Shengzhuang Town, and giant hail with a maximum diameter of 5 cm was observed on the ground, so the landing position and time of the identified giant hail are consistent with the ground reality (Fig. 2(a2)).

Figure 2(b2) shows that the large hail and giant hail identified by the modified HSDA have a reflectivity factor as low as 55 dBZ (Fig. 2(e)) at 1.5° elevation, since these heights are below the wet-bulb 0°C isotherm, and K_{DP} in most areas is above 1° km^{-1} (Fig. 2(h)), indicating that the hail began to melt and with abundant liquid water, with CC < 0.94 (Fig. 2(g)) and $Z_{DR} \approx 0$ dB (Fig. 2(f)). These results are consistent with the polarization characteristics of hail reported by Pan et al. (2021) and Diao et al. (2021). The sidelobe and three-body scattering characteristics at 1.5° and 2.4° elevation (data not shown) also indicate the existence of large hail with diameters greater than 2.5 cm (Lemon, 1998). Because of the attenuation caused by the strong echoes in front of zone A, the giant hail in zone A (Fig. 2(b2), marked by the red circle) has a larger area of negative Z_{DR} than in zone B (Fig. 2(f), marked by the red circle), otherwise due to the mixed-phase state or the complexity of hail shapes where the K_{DP} less than 0° km^{-1} in zone A, the giant hail in zone A (Fig. 2(b2), marked by the red circle) has smaller CC than in zone B (Fig. 2(g), marked by the red circle), but the small CC in the far end of zone A (Fig. 2(g), marked by the red lightning shape) may also be affected by three-body scattering.

4 Application of modified HSDA in a supercell hail process

To further verify the recognition effects of the improved HSDA and understand the developing trend of hail sizes in hailstorms, the improved HSDA is applied to a large acreage of the supercell hail process in Shandong Province. Affected jointly by the high-altitude cold vortex and the surface cyclone, the hailstorm broke out in 14 cities in Shandong from the afternoon to the night of May 17, 2020. The supercell storm produced severe hail, mainly in the eastern part of Weifang, Yantai, and Qingdao. According to witnesses and the disaster report, hail stones about 5 cm in diameter hit Changyi, Weifang at 19:57 BST, Chengyang, Qingdao at 20:25 BST, and Pingdu City at 20:31 BST. After 20:31 BST, hail stones about 6 cm in diameter fell on Laixi townships. The

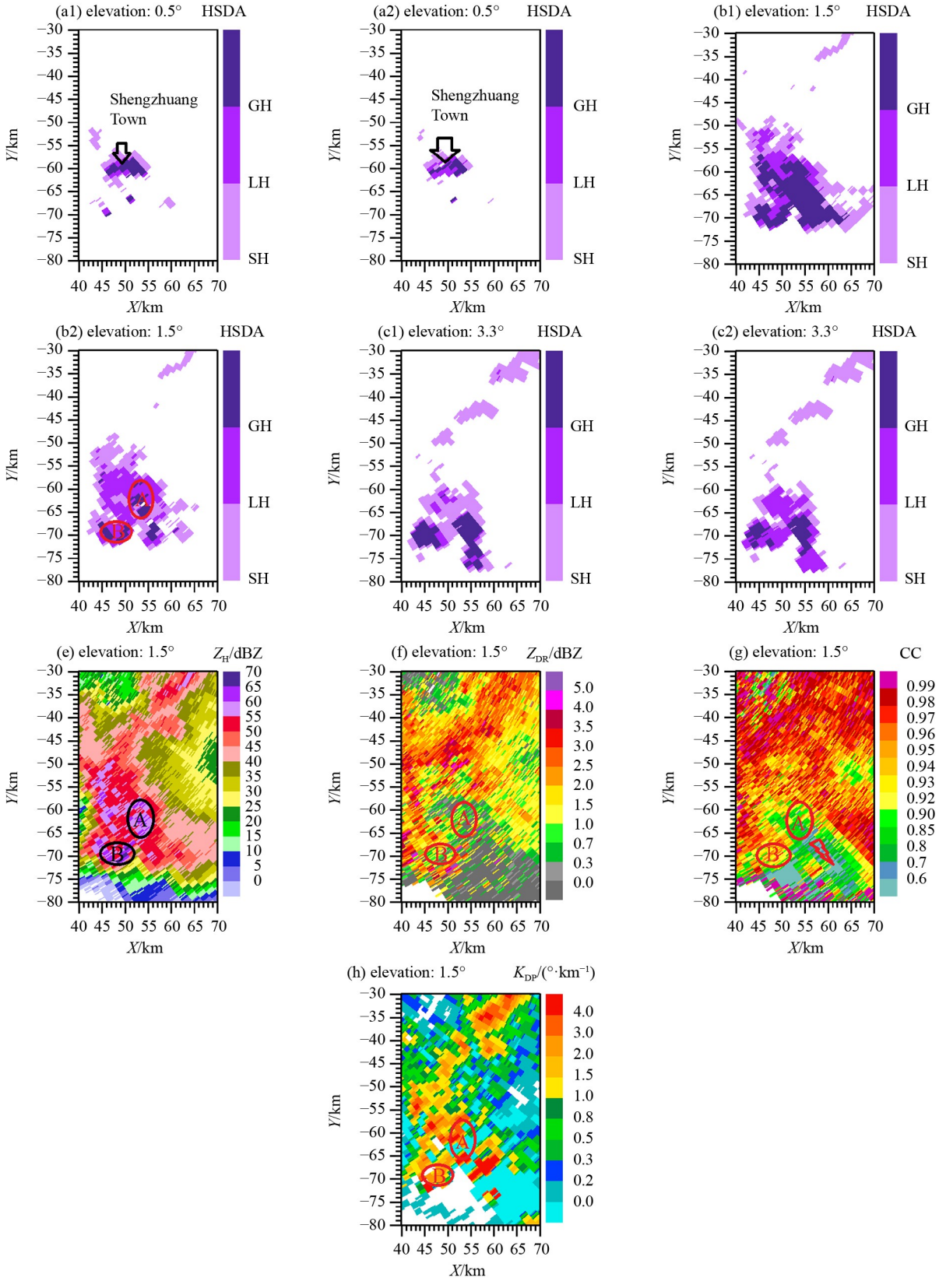

Fig. 2 The hail sizes detected by the HSDA proposed by Ortega et al. (2016) (panels (a1), (b1), and (c1) are 0.5°, 1.5°, and 3.3° elevation, respectively) and modified HSDA (panels (a2), (b2), and (c2) are 0.5°, 1.5°, and 3.3° elevation, respectively) with ΔZ_{DR} = −0.5 dB, and polarimetric parameters at 1.5° elevation (panels (e)–(h) are reflectivity factor Z_H, differential reflectivity factor Z_{DR}, correlation coefficient, and differential phase shift rate K_{DP}, respectively) of Jinan Radar at 18:05 on June 1, 2020 BST.

sounding data of Qingdao station at 20:00 BST show that the wet-bulb 0°C decreased to as low as 2.9 km.

4.1 Horizontal distribution characteristics of hail sizes

4.1.1 Identification results of different elevation angles of multiple hail cells

Figure 3 shows the Qingdao radar echo and the size of hail stones generated by storm cells at different elevation angles, as identified by the modified HSDA at 19:57 BST. Each cell is at a different stage of development, and cell B has developed into a supercell, while cell A will become a supercell due to the mesocyclone appearing in the next scan. The strong echo region exceeding 65 dBZ (Fig. 3(a)) of cells A and B generates giant hail and large hail (Figs. 3(b)). The giant hail is located on the strong-reflectivity side of the large gradient, while cells C–H mainly drop large and small hail (Figs. 3(b) and 3(c)), all of which is consistent with the hail report. The hail area of cell B (Fig. 3(d)) is as high as 8.5 km, which caused giant hail in Changyi City and Pingdu City during the moving process. Due to the attenuation of cell E, the back reflectivity factor of cell A significantly decreases to within 45 dBZ (Fig. 3(a)), resulting in a gap in hail identification (Fig. 3(b)).

4.1.2 Horizontal distribution of hail size and polarimetric parameters of hail of varying sizes

Figure 4 presents the polarimetric parameters at 0.5° elevation and the identification results of the hail size at various elevation angles from the Qingdao radar at 20:25 BST on May 17, 2020. Figure 4(f) reveals a large range of giant hail and large hail (about 2 km height) was falling to the ground, and large-area giant hail was generated at each elevation above the melting layer (Figs. 4(g)–4(i)) and reached a height of about 9.5 km (Fig. 4(i)), which is consistent with the hail sizes observed at 20:31 when giant hailstones were observed with a maximum diameter of 6 cm.

The large hail and giant hail (Fig. 4(f)) located near the mesocyclone (marked by the black circle labeled "M") appeared in front of the storm (Fig. 4(b)), and the giant hail was generated in the strong echo region with high gradient (inside the black frame) and fell near the mesocyclone (Figs. 4(a) and 4(b)) because the strong and rotating updraft can hold larger hail, while the smaller hail (large or small hail; Fig. 4(f)) is far from the strong updraft (Fig. 4(b)). Furthermore, the region with $K_{DP} > 3°$ km^{-1} (Fig. 4(e)) indicates that the hail melted and was accompanied by precipitation. Such a horizontal distribution of hail size is consistent with the filtering mechanism of supercell precipitation particles (Li, 2011).

The Z_{DR} of giant hail inside the black frame is around 0 dB (Fig. 4(c)) and presents negative values decreasing with increasing distance behind the strong echo core of 70 dBZ (Fig. 4(a)), which is mainly caused by the attenuation of horizontally and vertically polarized electromagnetic waves in the heavy hail area (Kumjian, 2013; Diao et al., 2021), otherwise, the CC is mainly between 0.8 and 0.9 (Fig. 4(d)) due to the mixed-phase state and complexity of hail shapes. The CC values in the area with below-60-dBZ reflectivity factor behind the black frame (Fig. 4(a)) decrease significantly (Fig. 4(d)) due to radar-beam broadening, which leads to non-uniform beam filling (NBF) of the particles with different shapes and phases.

4.2 Vertical distribution characteristics of hail sizes

Storm cell E reached maximum strength at 19:57 when the strongest echo center of more than 70 dBZ reached maximal height; the heaviest hail fell on the ground at about 20:31. Figure 5 shows the vertical profiles passing through the strong echo center of cell E at 19:57, then passing through the strong echo center at 0.5° elevation (20° azimuthal angle) from cell E at 20:31, and finally through the 20° azimuthal angle at 20:25.

4.2.1 Growth stage of heavy hails

At the time of heaviest hail growth, the strong echoes above 70 dBZ are more than 2 km above the −20°C isotherm (Fig. 5(a1)), and strong updrafts appear on the left side of the strong echo walls (Fig. 5(b1)). The maximum height of the Z_{DR} column (with large values exceeding 1 dB above the 0°C isotherm, where total length is expressed by depth) adjacent to the main updraft is above the −20°C isotherm (before interpolation, Fig. 5(d1)), with a depth of more than 4 km, meaning that large horizontal raindrops brought by strong updrafts provide conditions for the wet growth of hail. The extensive liquid water brought by the updrafts mainly distributes to the right of the Z_{DR} column, forming the K_{DP} column (with large values over 0.75 above the 0°C isotherm, as shown in Fig. 5(e1)). The maximum height of the K_{DP} column is also above the −20°C isotherm and the depth exceeds 3 km, which is the key area for large hail growth above the 0°C isotherm. When the hail falling velocity formed by the frost growth rate synchronizes with the updrafts, larger hailstones can grow and attain a height of over 5 km (Fig. 5(f1)) due to updrafts, forming an area of large gradient reflectivity (Fig. 5(a1)) above the bounded weak echo area. Therefore, the existence of giant hail and large hail (Fig. 5(f1)) between −10°C and −20°C is consistent with the key areas of wet growth of hail reported by Dennis and Musil (1973). Some large hail and giant hail rise to more than 9 km under the action of the updrafts (Fig. 5(f1)).

Large hail (Fig. 5(f1)) was generated in the Z_{DR} column, the presence of a few large liquid raindrops made

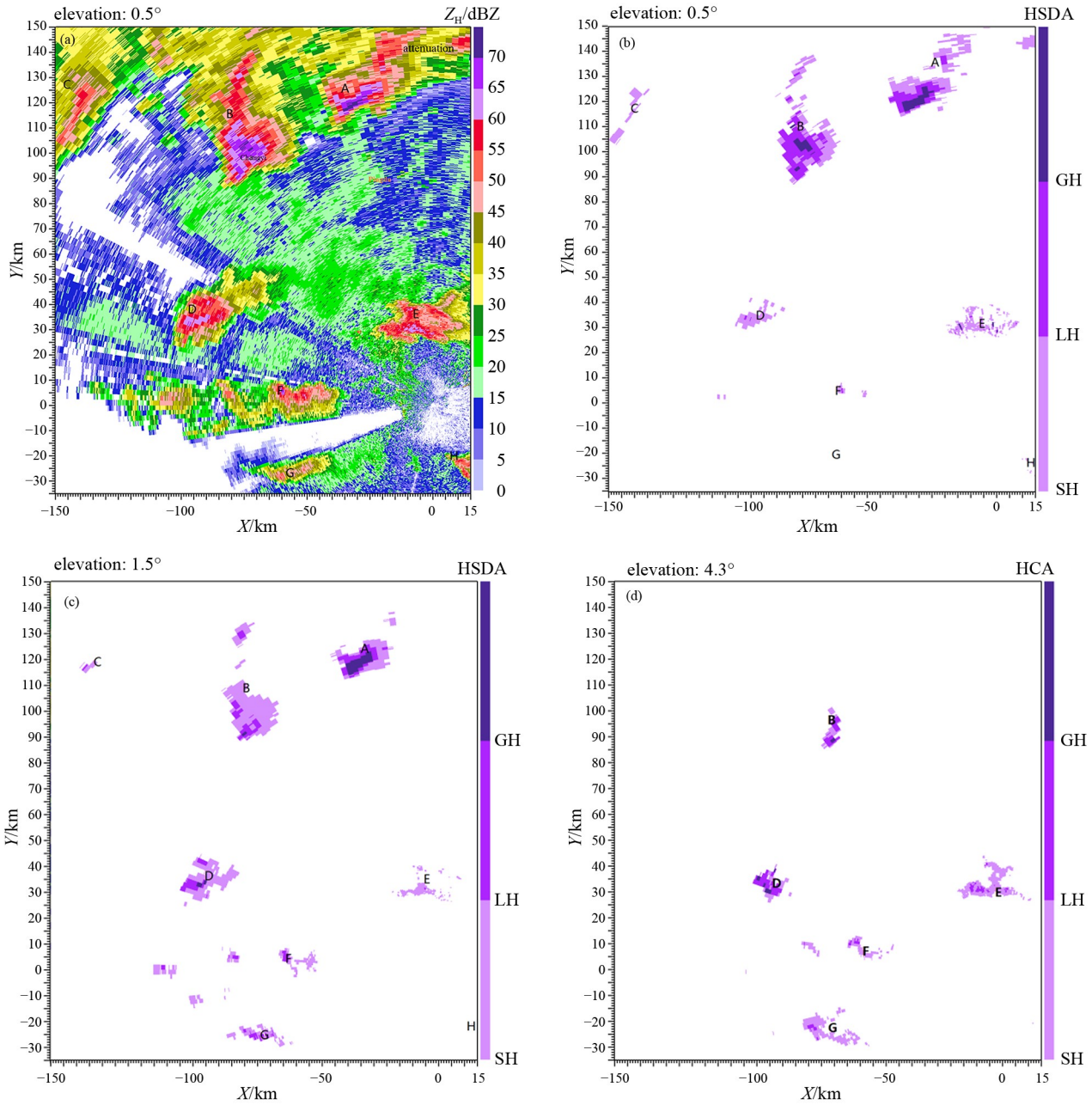

Fig. 3 Reflectivity factor at (a) 0.5° elevation, identification of hail size with ΔZ_{DR} = −0.5 dB at (b) 0.5° elevation, (c) 1.5° elevation, and (d) 4.3° elevation by Qingdao radar at 19:57 BST on May 17, 2020.

the K_{DP} value smaller (Fig. 5(e1)) in the Z_{DR} column, and the mixed-phase state produced CC ≈ 0.95 (Fig. 5(c1)). The giant hail near the updraft and within the K_{DP} column (Fig. 5(f1)) means that abundant supercooled water exists at this time, which provides favorable conditions for hail growth. Many large elliptic hailstones with vertical orientation may have determined the scattering characteristics of the particles in the irradiating volume, making Z_{DR} mainly negative (Fig. 5(d1)) and increasing CC (Fig. 5(c1)). The updrafts send the giant hail to a height of 9 km (Fig. 5(f1)), and the random orientation of the hail shows that Z_{DR} ≈ 0 dB (Fig. 5(d1)), and K_{DP} is reduced to about 0° km^{-1} (Fig. 5(e1)), indicating that the content of supercooled water decreased until it disappeared.

At the edge of the updrafts below 4 km, the large hail overcame the updrafts and started to fall (Fig. 5(b1)), while the small hail landed on the ground (Fig. 5(f1)), but a strong horizontal wind caused the velocity near the ground in the falling hail area to be oriented away from the radar (Fig. 5(b1)). Small hail (Fig. 5(f1)) was first generated in the suspended echo and was then injected into the growth area of larger hail under the updrafts and grew by colliding with abundant supercooled water in the

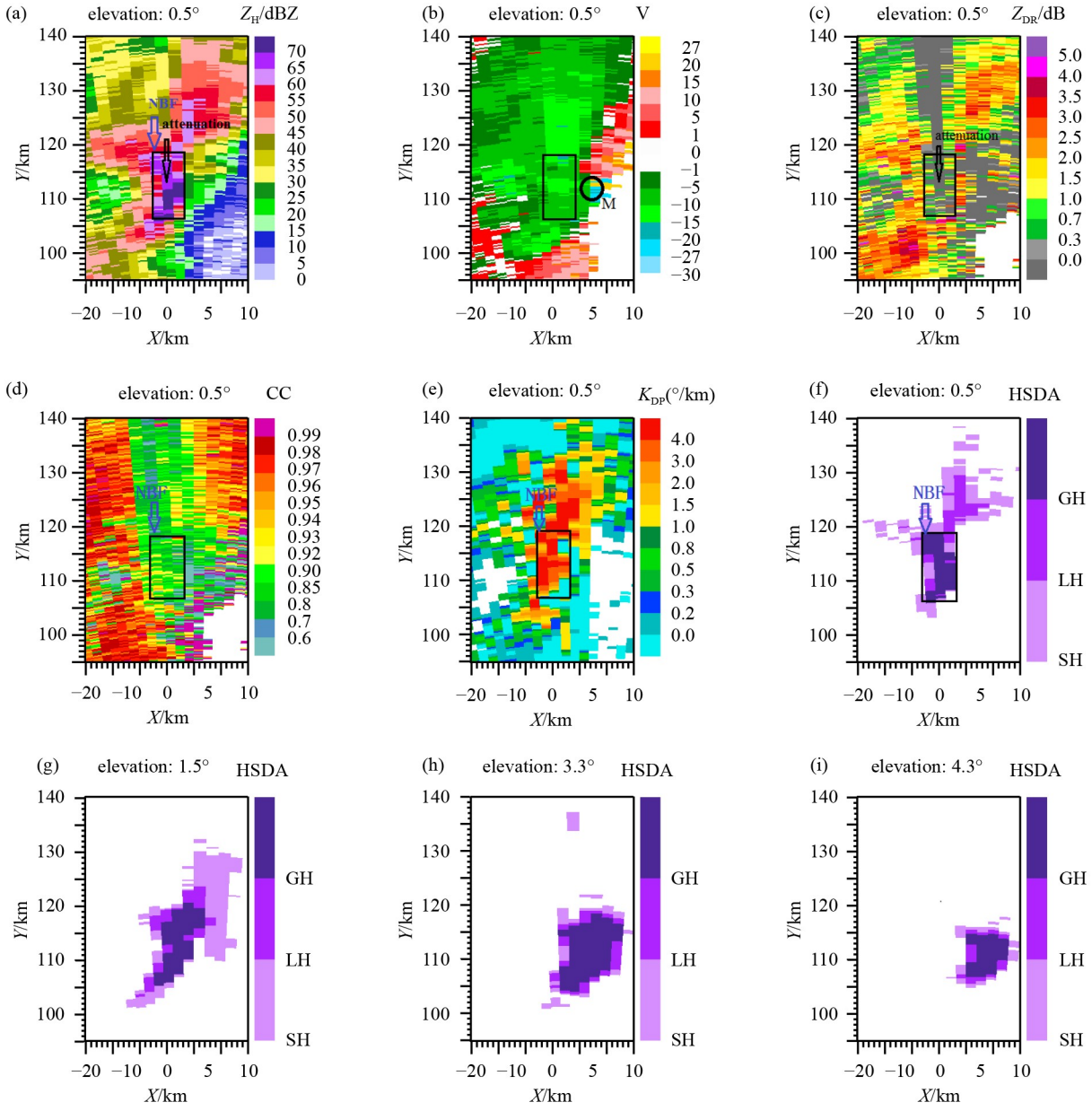

Fig. 4 (a) Z_H, (b) V, (c) Z_{DR}, (d) CC, and (e) K_{DP} at 0.5° elevation and the identification of hail size at (f) 0.5°, (g) 1.5°, (h) 3.3°, and (i) 4.3° elevation of the Qingdao radar at 20:25 BST on May 17, 2020.

K_{DP} column. The distribution of hail size is consistent with the growth mechanism of the supercell hail (Nelson, 1983; Xu and Duan, 2001; Gong et al., 2021).

4.2.2 Strong hail landing stage

For the volume scan before the strongest hail hit the ground, the maximum height of the Z_{DR} column indicates that the updraft intensity dropped below the −20°C isotherm (the height of the black arrow in Fig. 5(d2) indicates the maximum height of the Z_{DR} column after interpolation), and large hail emerged in the hanging echo, and a significant quantity of small hail and some large hail (Fig. 5(f2)) appeared on the strong-reflectivity side of the large gradient above the boundary weak echo reflectivity (BWER). The K_{DP} values near the Z_{DR} column decreased to below 0.8° km^{-1} (Fig. 5(e2)), indicating that the growth of hail consumed more supercooled water. The updrafts could no longer support the larger hail (Fig. 5(b2)), so the large hail and giant hail fell in close to the updraft to form a strong echo wall of more than 65 dBZ (Figs. 5(a2) and 5(a3)), while the small hail was falling away from the updrafts (Figs. 5(f2) and 5(f3)), which implies that the identification results are also consistent with the precipitation particle filtering mechanism of supercell storms (Li, 2011).

During the heaviest hails on the ground, the suspension echo, BWER (Fig. 5(a3)), and K_{DP} column all disappear

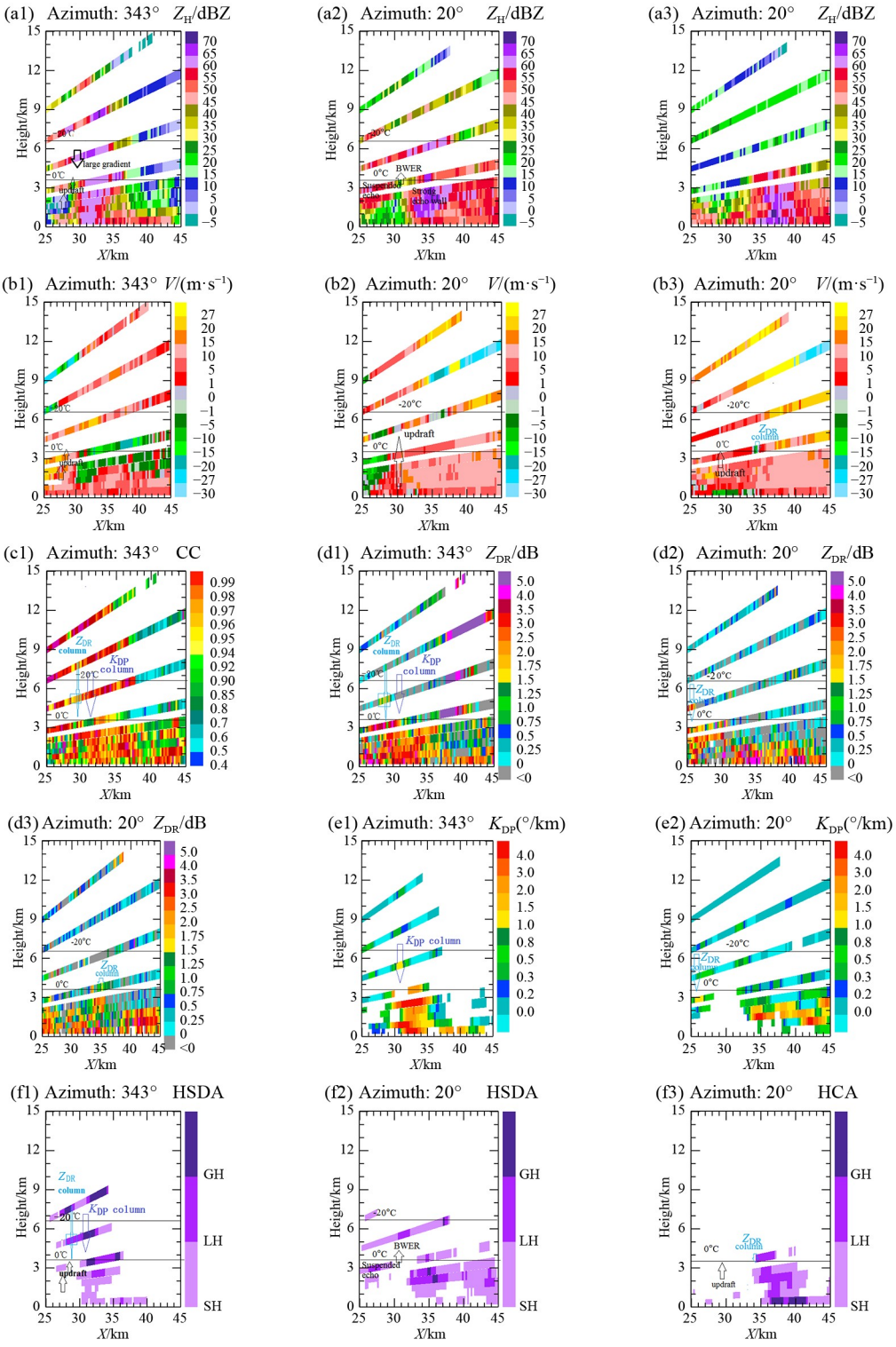

Fig. 5 Vertical profiles of (a1, a2) Z_H, (b1, b2) V, (c1) CC, (d1, d2) Z_{DR}, (e1, e2) K_{DP}, and (f1, f2) HSDA, along 343° azimuthal angle at 19:57 and 20° azimuthal angle at 20:25. Vertical profiles of (a3) Z_H, (b3) V, (d3) Z_{DR}, and (f3) HSDA, along 20° azimuthal angle at 20:31. All data acquired on May 17, 2020 BST from the Qingdao radar.

(image omitted), the top height of the Z_{DR} column continues to decrease (Fig. 5(d3), to a depth of 1 km), meaning that the updrafts were being weakened (Fig. 5(b3)), so the maximum height of the Z_{DR} column was predictive of the hail storm development, which is consistent with the results reported by Pan et al. (2021). Relative to the movement direction of the supercell, the giant hail fell on the edge of the main updrafts (Figs. 5(b2) and 5(b3)) within 6−12 km to the left and behind the updraft center (Fig. 5(f3)), which is consistent with

the area of giant hail studied by Witt et al. (2018).

5 Conclusions

The hail size discrimination algorithm (HSDA) based on the fuzzy logic principle and developed by Ortega et al. (2016) is discussed based on hail data acquired by the Shandong radars. The algorithm was localized because it was based on statistical hail data in Shandong. The improved membership function thresholds were obtained and applied to a multi-supercell hail process for verification.

1) Compared with the HSDA proposed by Ortega et al. (2016), the optimized HSDA mainly improves the identification of large hail and giant hail and improves the hail-size classification of all hail storm cells within the radar detection range. The results are entirely consistent with the analysis of the scattering and polarimetric parameters of hail of varying sizes, with the dynamics and microphysical characteristics of supercell hailstorms, and with the actual hail area and sizes.

2) The horizontal and vertical distributions of hail size provide insight into the growth process of larger hailstones and precipitation particle filtering mechanisms in supercells. In the growth stage of heavy hail, the maximum height of the Z_{DR} column and the K_{DP} column are both higher than the −20°C isotherm. Small hail was first generated in the hanging echo area and then injected into the growth area of larger hail under the action of updraft and grew through collisions with the abundant supercooled water in the K_{DP} column. Some hail, driven by the updrafts, rises above the −20°C isotherm and grows into giant hail. The large hail and giant hail fell near the updrafts to form a strong echo wall of more than 65 dBZ, while the small hail fell away from the updrafts. The giant hail fell on the edge of the main updrafts within 6–12 km from the updraft center.

3) The evolution of the maximum height of the Z_{DR} and K_{DP} columns is indicative of the hail storm development. In the high-altitude growth stage of supercell hail, the Z_{DR} and K_{DP} column depths can exceed 4 and 3 km, respectively. However, when heavy hail falls to the ground, the Z_{DR} depth drops to 1 km and the K_{DP} column disappears because the hail growth consumed excessive supercooled water.

4) Hail size in a hail region was first determined by using the HCA (Park et al., 2009), so the identification range of the small hail depends mainly on the HCA. Radar data quality affects the algorithm results due to electromagnetic interference, beam blocking, etc. The above echoes are avoided, and simple quality control is carried out in this paper. The attenuation caused by strong hail cells can reduce the reflectivity factor and Z_{DR}, so the HCA and HSDA may misidentify those hail areas. At present, the algorithm is mainly used to verify finite processes. Considering the complexity of hailstone processes, it is hoped that further study will focus on reducing error and implementing statistical verification. The phenomenon is that the CC values behind the strong echo core are sometimes large and sometimes small, which is also worthy of further study.

Acknowledgments This study was supported by the Shandong Provincial Natural Science Foundation of China (Nos. ZR2020MD052 and ZR2022MD072), the National Natural Science Foundation of China (Grant No. 41675029), East China Regional Collaborative Innovation Fund for Meteorological Science and Technology (No. QYHZ202101), Project of Xiamen Bureau of Science and Technology (No. 3502Z20214ZD4005), Key Project of Shandong Meteorological Bureau (Nos. 2021SDQXZ09 and SDLD2022-02)

Competing interests The authors declare that they have no competing interests.

References

Al-Sakka H, Boumahmoud A A, Fradon B, Frasier S J, Tabary P (2013). A new fuzzy logic hydrometeor classification scheme applied to the French X-, C-, and S-band polarimetric radars. J Appl Meteorol Climatol, 52(10): 2328–2344

Dennis A S, Musil D J (1973). Calculations of hailstone growth and trajectories in a simple cloud Model. J Atmos Sci, 30(2): 278–288

Diao X, Guo F (2021). Structure characteristics of dual polarization parameters of Zhucheng supercell storm on August 16, 2019. Acta Meteorol Sin, 79(2): 181–195

Diao X, Huang X, Ren Z, Yang C, Liu Z, Geng L, Zhu J (2007). Verification and parameter localization of CINRAD/SA radar hail detection algorithm. Meteorol Sci Techn, 35(5): 727–731

Diao X, Yang C, Zhang Q, Lu Q (2021). Analysis on the evolution characteristics of storm parameters and Z_{DR} column for two long life supercells. Plateau Meteorol, 40(3): 580–589

Dolan B, Rutledge S A (2009). A theory-based hydrometeor identification algorithm for x-band polarimetric radars. J Atmos Ocean Technol, 26(10): 2071–2088

Gong D, Wang H, Xu H, Wang W, Zhu J, Wang J (2021). Observational analysis of a rare and severe hailstorm cloud structure and large hailstones formation on 16 August 2019 in Zhucheng, Shandong province. Acta Meteorol Sin, 79(4): 674–688

Heinselman P L, Ryzhkov A V (2006). Validation of polarimetric hail detection. Weather Forecast, 21(5): 839–850

Kaltenboeck R, Ryzhkov A (2013). Comparison of polarimetric signatures of hail at S and C bands for different hail sizes. Atmos Res, 123: 323–336

Kumjian M R (2013). Principles and applications of dual-polarization weather radar. Part III: artifacts. J Operat Meteorol, 1(21): 265–274

Lemon L R (1998). The radar “Three-body scatter spike”: an operational large-hail signature. Weather Forecast, 13(2): 327–340

Li B (2011). Weather Radar and Its Application. Beijing: China Meteorological Press, 243–256

Lin W, Zhang S, Luo C, Jiang H, Xie Z, Li D, Chen B (2020). Observational analysis of different intensity sever convective clouds

by S-band dual-polarization radar. Meteor Monthly, 46(1): 63–72 (in Chinese)

Nelson S P (1983). The influence of storm flow structure on hail growth. J Atmos Sci, 40(8): 1965–1983

Ortega K L, Krause J M, Ryzhkov A V (2016). Polarimetric radar characteristics of melting hail. Part III: validation of the algorithm for hail size discrimination. J Appl Meteorol Climatol, 55(4): 829–848

Pan J, Guo L, Wei M, Luo R, Gao L, Zheng X, Peng Y (2021). Analysis of the polarimetric characteristics of hail storm from S band dual polarization radar observations. Acta Meteorol Sin, 79(1): 168–180

Pan J, Wei M, Guo L, Yan Y, Luo C, Wu L (2020). Dual polarization radar characteristic analysis of the evolution of heavy hail supercell in Southern Fujian. Meteor Month, 46(12): 1608–1620 (in Chinese)

Park H S, Ryzhkov A V, Zrnić D S, Kim K E (2009). The hydrometeor classification algorithm for the polarimetric wsr-88d: description and application to an MCS. Weather Forecast, 24(3): 730–748

Ryzhkov A V, Kumjian M R, Ganson S M, Khain A P (2013a). Polarimetric radar characteristics of melting hail. Part I: theoretical simulations using spectral microphysical modeling. J Appl Meteorol Climatol, 52(12): 2849–2870

Ryzhkov A V, Kumjian M R, Ganson S M, Zhang P (2013b). Polarimetric radar characteristics of melting hail. Part II: practical implications. J Appl Meteorol Climatol, 52(12): 2871–2886.

Scharfenberg K A, Miller D J, Schuur T J, Schlatter P T, Giangrande S E, Melnikov V M, Burgess D W, Andra D L Jr, Foster M P, Krause J M (2005). The joint polarization experiment: polarimetric radar in forecasting and warning decision making. Weather Forecast, 20(5): 775–788

Snyder J C, Ryzhkov A V, Bluestein H B, Scott F B (2014). Polarimetric analysis of two giant-hail-producing supercells observed by X-band and S-band radars. In: 27th Conf on Severe Local Storms, Madison, Amer Meteor Soc, 166

Tang L, Zhang J, Langston C, Krause J, Howard K, Lakshmanan V (2014). A physically based precipitation-nonprecipitation radar echo classifier using polarimetric and environmental data in a real-time national system. Weather Forecast, 29(5): 1106–1119

Wang H, Wu N, Wan Q, Zhan C (2018). Analysis of s-band polarimetric radar observations of a supercell storm in south China. Acta Meteorol Sin, 76(1): 92–103

Witt A, Burgess D W, Seimon A, Allen J T, Snyder J C, Bluestein H B (2018). Rapid-scan radar observations of an Oklahoma tornadic hailstorm producing giant hail. Weather Forecast, 33(5): 1263–1282

Witt M, Eilts D, Stumpf G J, Johnson J T, Mitchell E D W, Thomas K W (1998). An enhanced hail detection algorithm for the WSR-88D. Weather Forecast, 13(2): 286–303

Wu C, Liu L, Wei M, Xi B, Yu M (2018). Statistics-based optimization of the polarimetric radar hydrometeor classification algorithm and its application for a squall line in south China. Adv Atmos Sci, 35(3): 296–316

Wu J, Pan J, Wei M, Gu Y (2022). Statistics of polarization characteristics of hail at different scales by S-band dual-polarization radar. J Trop Meteorol, 38(2): 161–170

Xia F, Zhang L, Zhang L (2021). Study of recognition algorithm of non-precipitation echo for Beijing X-band radar based on dual polarization parameter. Meteoro Month, 47(5): 561–572 (in Chinese)

Xu H, Duan Y (2001). The mechanism of hailstone's formation and the hail-suppression hypothesis: "Beneficial Competition". Chin J Atmos Sci, 25(2): 277–288

Yu X (2014). Melting layer height of hail. Meteoro Month, 40(6): 649–654 (in Chinese)

Zeng Z, Chen Y, Zhu K, Li S (2019). Characteristics of atmospheric stratification and melting effect of heavy hail events in Guangdong Province. Chin J Atmos Sci, 43(3): 598–617

Zrnić D, Ryzhkov A (1999). Polarimetry for weather surveillance radars. Bull Am Meteorol Soc, 80(3): 389–406